Research Article

# Predicting Human Tissue Exposures to Xenobiotics Using a Bottom-up Physiologically-Based Biokinetic Model

*Shawn P. F. Tan*[1,2], *Eric C. Y. Chan*[2,3] *and James C. Y. Chan*[1,2,4]

[1]Skin Research Institute of Singapore, Agency for Science Technology and Research, Singapore; [2]Innovations in Food and Chemical Safety, Agency for Science Technology and Research, Singapore; [3]Department of Pharmacy, National University of Singapore, Singapore; [4]Singapore Institute of Food and Biotechnology Innovation, Agency for Science, Technology and Research, Singapore

**Abstract**

Advances in physiologically-based biokinetic (PBK) modelling, *in vitro*-to-*in vivo* extrapolation (IVIVE) methodologies, and development of permeability-limited biokinetic models have allowed predictions of tissue drug concentrations without utilizing *in vivo* animal or human data. However, there is a lack of *in vivo* human tissue concentrations to validate these models. Herein, we validated the performance of our previously published bottom-up rosuvastatin (RSV) PBK model with clinical data from a recently published study that made use of positron emission tomography (PET) imaging to quantify the hepatic concentrations of [$^{11}$C]RSV drug-drug interaction (DDI) with cyclosporine A (CsA). Simulated RSV area under the plasma concentration-time curve ($AUC_{0h\text{-}t}$) and maximum plasma concentration ($C_{max}$) before and after DDI were within 1.5-fold of the observed data. Simulated $AUC_{0\text{-}30min}$ and $C_{max}$ ratios in the DDI setting matched the observed ratios closely (within 1.1-fold). To predict RSV hepatic concentrations, the model inputs were modified to account for RSV in the bile canaliculi after biliary excretion. The model recapitulated the observed hepatic concentrations before DDI and the decrease in hepatic concentrations after DDI. Simulated area under the liver concentration-time curve ($AUC_{0\text{-}30min,liver}$), maximum liver concentration ($C_{max,liver}$), $AUC_{0\text{-}30min,liver}$ ratio and $C_{max,liver}$ ratios were predicted within 1.5-fold of the observed data. In summary, we validated the ability of bottom-up PBK modelling to predict RSV hepatic concentrations with and without DDI with CsA. Our findings confirm the importance to account for drug distributed within the bile canaliculi for accurate prediction of hepatic tissue drug levels when compared against *in vivo* liver PET scan data.

## 1 Introduction

A quantitative understanding of the free or unbound concentrations of a chemical compound within various tissues of the body is necessary to fully appreciate its pharmacodynamic or toxicodynamic potential (Chu et al., 2013). It is accepted that only the intracellular unbound fraction of a biologically active compound interacts with its molecular target, driving the potential for efficacy or toxicity. In the pharmaceutical sector, where clinical studies using human subjects are performed frequently, the unbound plasma concentration (measured plasma concentration multiplied by fraction unbound ($f_{u,p}$)) is frequently assumed to be a surrogate measure of unbound tissue concentrations (Ryu et al., 2020). However, this relies on the assumption of the free drug/chemical hypothesis, which is invalid for compounds with poor passive permeability where tissue concentrations are modulated by either active uptake or efflux membrane transporters (Zhang et al., 2019a). For certain compounds, it has been found that the steady-state ratio of unbound tissue concentrations against unbound plasma concentration ($K_{p,uu}$) can be much greater than one, indicating tissue accumulation. For example, the rosuvastatin (RSV) liver $K_{p,uu}$ ($K_{p,uu,liver}$) was estimated to be 57, representing a 57-fold higher unbound RSV concentration in the liver versus plasma (Zhang et al., 2019b). Therefore, the unbound plasma concentration can be an inappropriate measure of the unbound tissue concentrations. Conventionally, intracellular unbound concentrations are assessed by harvesting tissues of animals dosed with the compound of interest. However, with the

Received July 15, 2020; Accepted November 6, 2020;
Epub November 9, 2020; © The Authors, 2021.

**ALTEX 38(2), 253-268.** doi:10.14573/altex.2007151

Correspondence: James Chun Yip Chan, PhD
Singapore Institute of Food and Biotechnology Innovation
Agency for Science, Technology and Research
31 Biopolis Way, #01-02 Nanos, Singapore 138669
(James_Chan@sifbi.a-star.edu.sg)

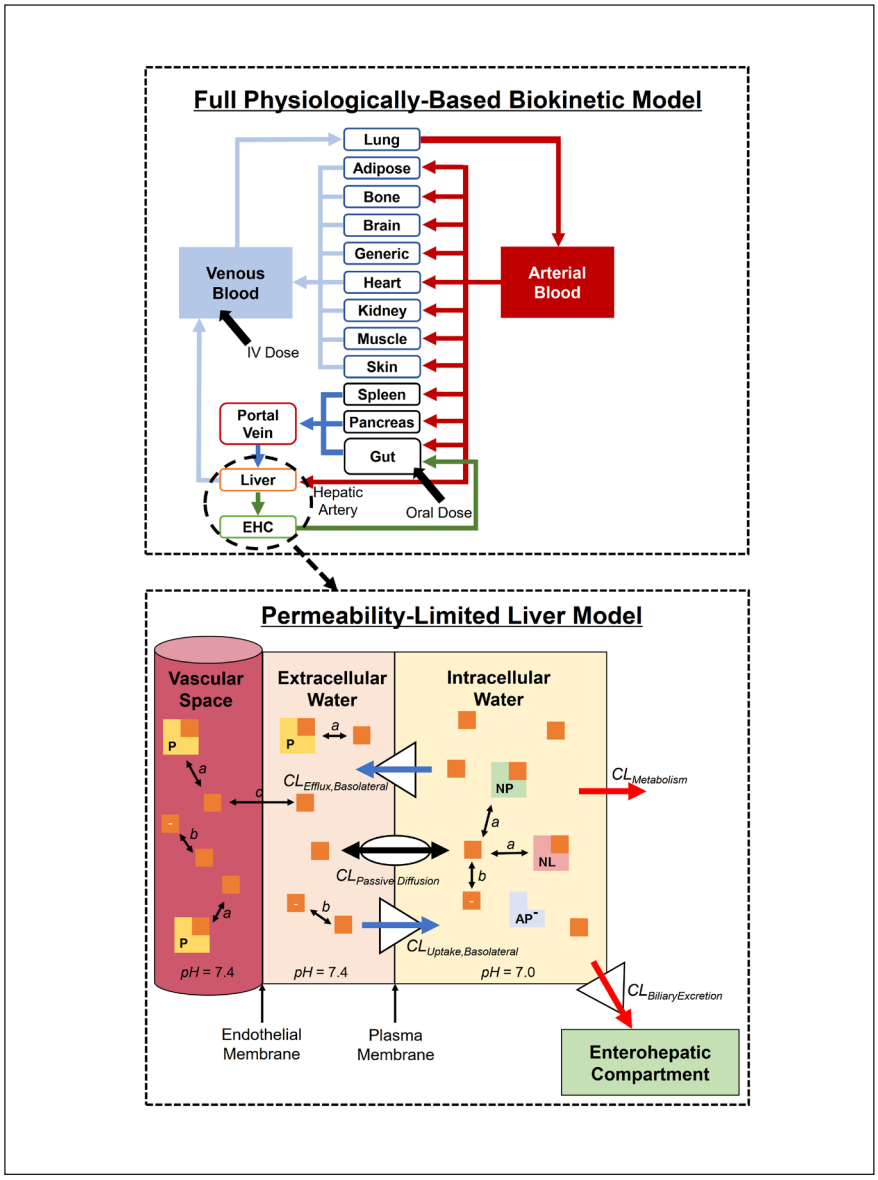


**Fig. 1: Full physiologically-based biokinetic model framework used within Simcyp® to simulate the plasma and organ tissue concentration-time profile, including the associated permeability-limited liver model used to describe the hepatic distribution of rosuvastatin between the vascular space (VS), extracellular water (EW) and intracellular water (IW) compartments**

The VS consists of blood supply arriving from the portal vein and hepatic artery. Distribution of the unbound, unionized compound between the VS and EW is instantaneous, while the distribution between the EW and IW would depend on the rate of passive diffusion ($CL_{PassiveDiffusion}$), active uptake ($CL_{Uptake,Basolateral}$), and active efflux ($CL_{Efflux,Basolateral}$). Elimination of the unbound compound from the IW would depend on the rate of metabolism ($CL_{Metabolism}$) and rate of biliary excretion ($CL_{BiliaryExcretion}$). The fraction unbound in the intracellular water ($fu_{IW}$) is influenced by the binding of the compound to intracellular neutral phospholipids (NP), neutral lipids (NL), and acidic phospholipids (AP). The three equilibrium processes refer to (a) binding to plasma protein, NP, NL and AP, (b) ionization of the compound, and (c) instantaneous equilibrium of unbound, unionized compound between the VS and EW.

growing shift towards non-animal testing methods for risk assessment of chemicals, there is a need for alternative methods to obtain unbound chemical concentrations in human tissues. This in turn has driven the development of various *in silico* methods to obtain unbound tissue concentrations, such as physiologically-based biokinetic (PBK) modelling.

PBK modelling, also commonly described as physiologically-based pharmacokinetic/toxicokinetic (PBPK/PBTK) modelling, utilizes an anatomically and physiologically accurate mathematical representation of the human body to predict the biokinetics of chemical compounds. It incorporates key parameters, such as tissue volumes, blood flow, protein binding, and metabolic enzyme and transporter expression levels that influence the absorption, distribution, metabolism and excretion (ADME) of chemicals. PBK models can be parameterized with *in vitro* biokinetic measurements to permit *in vitro*-to-*in vivo* extrapolation (IVIVE) for the prediction of human ADME parameters. Importantly, using appropriate scaling factors, one can robustly predict the plasma concentration time-course using purely *in vitro* data (bottom-up approach). We have recently published an example illustrating this approach using three metabolism- and transporter-dependent compounds (RSV, fluvastatin and pitavastatin) (Chan et al., 2019).

Besides predicting plasma concentrations, recent advances in PBK modelling have led to the development of permeability-limited biokinetic models for specific organs that have significantly improved the IVIVE of transporter-dependent compounds. Such models have been developed for different organs including the liver and kidney (Jamei et al., 2014; Steffansen et al., 2015; Huang and Isoherranen, 2018). Permeability-limited

biokinetic models divide the organ into three compartments: intracellular, extracellular and vascular space. An example of a permeability-limited model for the liver is illustrated in Figure 1. Typically, it is assumed that blood capillaries do not present a barrier to small molecule solutes; hence the unbound, unionized compound undergoes instantaneous equilibrium between the vascular and extracellular space. From the extracellular space, the unbound compound crosses the biological membrane barrier via passive diffusion, transporter-mediated uptake or both. Within the intracellular compartment, the unbound compound can exit the cell through passive diffusion and transporter-mediated efflux back into the extracellular space via the basolateral membrane or be excreted via the apical membrane. Additionally, it may undergo metabolic clearance in the intracellular compartment. In each compartment, the fraction of each chemical that is free or unbound is a critical parameter that influences the kinetics of all these processes. The structure of such permeability-limited biokinetic models allows for mechanistic modelling of the concentration and time-course of permeability-limited compounds in the intracellular and extracellular compartments. The use of permeability-limited biokinetic models, parameterized by *in vitro* passive and active transport data, has significantly improved the predictions of plasma concentrations (Chan et al., 2019).

While it is possible to predict tissue concentrations using these models, the major challenge lies in obtaining relevant *in vivo* human tissue concentrations for model validation. Quantitative imaging methods such as positron emission tomography (PET), contrast enhanced magnetic resonance imaging, and γ-scintigraphy may be used to measure tissue concentrations (Guo et al., 2018). Due to the cost of conducting clinical imaging studies, such studies are not routinely performed. Instead, it has been suggested that quantitative imaging of a small number of probe transporter substrates may be performed to validate and refine existing PBK models and build confidence in the predictions of tissue concentrations (Guo et al., 2018; Billington et al., 2019).

In 2019, a landmark study published by Billington et al. utilized PET imaging to quantify the concentrations of [$^{11}$C]RSV in various organs including the liver and kidney with and without drug-drug interaction (DDI) with cyclosporine A (CsA) (Billington et al., 2019). This was a first-of-its kind study that provided crucial *in vivo* tissue level data needed to validate predictions of hepatic RSV concentrations in humans. As a compound with high solubility but poor metabolism and permeability, RSV is classified as a Biopharmaceutics Drug Disposition Classification System (BDDCS) class 3 compound (Benet et al., 2011). As a result, elimination of RSV relies on hepatic uptake transporters. It is an FDA recommended probe substrate for hepatic uptake transporters such as organic-anion transporting polypeptide 1B1 and 1B3 (OATP1B1 and OATP1B3) and efflux transporters such as breast cancer resistant protein (BCRP) (US Food and Drug Adminstration, 2020). Thus, RSV is an ideal compound to study the effect of transporters on modulating intracellular hepatic concentrations. Furthermore, it undergoes minimal metabolism, reducing confounding effects from possible metabolites of [$^{11}$C]RSV when quantifying hepatic [$^{11}$C]RSV concentrations from PET scan images. This is because PET imaging is unable to discriminate between signals arising from the parent [$^{11}$C]RSV and its metabolite (Kaneko et al., 2018). Finally, as CsA is a validated clinical probe inhibitor of OATP1B1, OATP1B3 and BCRP transporters, it allows an assessment of the impact of transporter-level interactions on RSV hepatic concentrations (US Food and Drug Adminstration, 2020). The results from the PET imaging study afforded a unique opportunity to validate the ability of our previously published proteomics-informed bottom-up PBK model of RSV to predict hepatic concentrations (Chan et al., 2019).

In the present study, we made use of our previously published model of RSV and integrated it with a middle-out PBK model of CsA modified with updated transporter inhibitory constant ($K_i$) values. First, we performed a validation of the PBK models in predicting the plasma concentrations of RSV and CsA separately. A second level of validation was performed by predicting RSV plasma concentrations during a DDI with CsA. Subsequently, we applied our models to simulate the hepatic concentrations of RSV alone, as well as after DDI with CsA, using [$^{11}$C]RSV PET imaging data to validate the predicted tissue biokinetic profiles. The results of our simulations demonstrate that by using a permeability-limited liver model incorporating extensive transporter uptake, efflux and inhibition kinetics, we are able to robustly predict both plasma and hepatic concentrations of RSV before and after DDI with CsA. Finally, the model was applied to predict the $K_{p,uu,liver}$ of rosuvastatin and to perform a pharmacokinetic/pharmacodynamic (PK/PD) correlation for the lowest clinically used dose of RSV. To the best of our knowledge, this is the first study in which a bottom-up PBK model has been validated to predict both human plasma and hepatic concentrations for a transporter-dependent compound. The results of our study will build further confidence in the ability of bottom-up PBK modelling as an alternative to animal testing to predict both plasma and tissue biokinetics.

## 2 Materials and methods

### 2.1 Model development

*PBK model of RSV*

The population-based ADME Simcyp® simulator (Version 18, Release 1, Certara UK Ltd, Simcyp Division, Sheffield, UK) was used to develop all our PBK models. Compound-dependent input parameters for RSV are found in Table 1. The PBK model of RSV was identical to the bottom-up model we published previously (Chan et al., 2019). Briefly, the full PBK model was used to describe the perfusion-limited distribution of RSV into various organ compartments. The Rodgers and Rowland (2007) tissue composition method was used to predict the tissue-to-plasma equilibrium distribution ratios for each organ compartment. The permeability-limited liver (PerL) model was incorporated into the full PBK model (Fig. 1) to describe the permeability-limited distribution of RSV into the liver (Jamei et al., 2014). The PerL model divides the liver into 3 compartments: intracellular

water (IW), extracellular water (EW) and vascular space (VS). It is assumed that unbound, unionized compounds within the EW and VS are in instantaneous equilibrium, and the distribution between both compartments through the capillary barrier is not a rate-limiting process. In contrast, distribution between the EW and IW is governed by the compound's passive and active transport across the plasma membrane. Several transporters facilitate the saturable uptake of RSV at the basolateral membrane from the EW to IW: OATP1B1, OATP1B3, OATP2B1 and sodium-taurocholate co-transporting polypeptide (NTCP) (Chan et al., 2019). Conversely, multidrug resistance-associated protein 4 (MRP4) is responsible for the efflux of RSV back into the EW from the IW at the basolateral membrane. At the canalicular membrane, two efflux transporters are responsible for the excretion of RSV into the bile canaliculi, BCRP and possibly P-glycoprotein (P-gp). An overall canalicular efflux intrinsic clearance ($CL_{int}$) was used to define the transporter-mediated biliary clearance of RSV in the model (Chan et al., 2019).

**Tab. 1: PBK model input parameters of RSV**
Retrieved from Chan et al. (2019).

| Parameter | Value | Method/reference |
|---|---|---|
| Molecular weight (g/mol) | 481.54 | Jamei et al., 2014 |
| log P | 2.4 | Jamei et al., 2014 |
| Compound type | Monoprotic acid | |
| pKa | 4.27 | Jamei et al., 2014 |
| B/P | 0.625 | Jamei et al., 2014 |
| $f_{u,p}$ | 0.107 | Jamei et al., 2014 |
| Main plasma binding protein | Human serum albumin | |
| **Absorption** | | |
| $fu_{gut}$ | 1 | |
| $P_{eff,man}$ ($10^{-4}$ cm/s) | 0.1843941 | Predicted in Simcyp Sun et al., 2002 |
| Permeability assay | Caco-2 | |
| Apical pH : basolateral pH | 7.4 : 7.4 | |
| Activity | Passive & active | |
| $P_{appA:B}$ ($10^{-6}$ cm/s) | 0.4 | Li et al., 2011 |
| Reference compound | Propranolol | |
| Reference compound $P_{appA:B}$ ($10^{-6}$ cm/s) | 43 | Li et al., 2011 |
| Scalar | 1 | |
| **Distribution** | | |
| Distribution model | Full PBK model | |
| $V_{SS}$ (L/kg) | 0.1178358 | Predicted in Simcyp using Method 2<br>Rodgers et al., 2005; Rodgers and Rowland, 2006 |
| Predicted tissue:plasma partition coefficients | | |
| Adipose | 0.052 | |
| Bone | 0.116 | |
| Brain | 0.083 | |
| Gut | 0.190 | |
| Heart | 0.193 | |
| Lung | 0.246 | |
| Muscle | 0.069 | |
| Skin | 0.319 | |
| Spleen | 0.134 | |
| Pancreas | 0.096 | |
| **Metabolism** | | |
| Enzyme | CYP3A4 | |
| Pathway | Pathway 1 | |
| $CL_{int}$ (µL/min/mg protein) | 1.1 | Fujino et al., 2004 |
| $fu_{mic}$ | 0.937 | Simcyp Prediction Toolbox |
| Enzyme | UGT 1A1 | |
| Pathway | Pathway 1 | |
| $V_{max}$ (pmol/min/mg protein) | 17 | Schirris et al., 2015 |
| $K_m$ (µM) | 16 | Schirris et al., 2015 |
| rUGT scalar | 0.92 | Simcyp Database |
| Enzyme | UGT 1A3 | |
| Pathway | Pathway 1 | |
| $V_{max}$ (pmol/min/mg protein) | 105 | Schirris et al., 2015 |
| $K_m$ (µM) | 220 | Schirris et al., 2015 |
| rUGT scalar | 1 | |
| **Permeability limited liver model** | | |
| $CL_{PD}$ (µL/min/million hepatocytes) | 0.0025 | Jamei et al., 2014 |
| $fu_{IW}$ | 0.9673012 | Predicted<br>Jamei et al., 2014 |
| $fu_{EW}$ | 0.1869325 | Predicted<br>Jamei et al., 2014 |
| Transporter | SLC10A1 (NTCP) | |
| $CL_{int,T}$ (µL/min/million) | 3.4 | Bi et al., 2013 |
| RAF/REF | 1.353 | Chan et al., 2019 |
| Transporter | SLCO1B1 (OATP1B1) | |
| $J_{max}$ (pmol/min/million) | 103 | Izumi et al., 2018 |
| $K_m$ (µM) | 9.31 | Izumi et al., 2018 |
| RAF/REF | 8.656 | Chan et al., 2019 |

| Permeability limited liver model | | |
|---|---|---|
| Transporter | SLCO1B3 (OATP1B3) | |
| $J_{max}$ (pmol/min/million) | 111.3 | Bosgra et al., 2014 |
| $K_m$ (µM) | 16.5 | Bosgra et al., 2014 |
| RAF/REF | 8.036 | Chan et al., 2019 |
| Transporter | SLCO2B1 (OATP2B1) | |
| $J_{max}$ (pmol/min/million) | 17.3 | Bosgra et al., 2014 |
| $K_m$ (µM) | 26.1 | Bosgra et al., 2014 |
| RAF/REF | 100 | Chan et al., 2019 |
| Transporter | ABCC4 (MRP4) | |
| $J_{max}$ (pmol/min/million) | 1140 | Pfeifer et al., 2013 |
| $K_m$ (µM) | 21 | Pfeifer et al., 2013 |
| RAF/REF | 0.028 | Chan et al., 2019 |
| Transporter | Canalicular efflux (liver) | |
| $CL_{int,T}$ (µL/min/million) | 1.5 | Jones et al., 2012 |
| RAF/REF | 1.611 | Chan et al., 2019 |

| Mechanistic kidney model | | |
|---|---|---|
| $CL_{PD,basal}$ (mL/min/million proximal tubular cells) | 0.00507 | Verhulst et al., 2008 |
| $CL_{PD,apical}$ (mL/min/million proximal tubular cells) | 0.00507 | Verhulst et al., 2008 |
| $fu_{kidney,cell}$ | 0.985129 | Predicted in Simcyp<br>Rodgers et al., 2005; Rodgers and Rowland, 2006 |
| $fu_{urine}$ | 1 | |
| Transporter | SLC22A8 (OAT3) | |
| Function | Uptake | |
| $J_{max}$ (pmol/min/million cells) | 546 | Verhulst et al., 2008 |
| $K_m$ (µM) | 20.4 | Verhulst et al., 2008 |
| Transporter | ABCC4 (MRP4) | |
| Function | Efflux | |
| $J_{max}$ (pmol/min/million cells) | 546 | Verhulst et al., 2008 |
| $K_m$ (µM) | 20.4 | Verhulst et al., 2008 |

*PBK model of CsA*

Physicochemical properties and metabolism kinetics of CsA were adopted from the Simcyp compound file library. Compound-dependent input parameters for CsA are found in Table 2. Similar to RSV, the full PBK model and Rodgers and Rowland method were used to describe perfusion-limited tissue distribution. CsA is an inhibitor of several transporters involved in the transport of RSV. $K_i$ values of CsA for the inhibition of OATP1B1, OATP1B3, OATP2B1, NTCP and BCRP were obtained from the literature and applied to the model (Jamei et al., 2014; Vildhede et al., 2014; Wang et al., 2017). To permit inhibition of canalicular efflux of RSV, $K_i$ of CsA for the inhibition of BCRP was used as the input parameter.

**Tab. 2: PBK model input parameters of CsA**

| Parameter | Value | Method/reference |
|---|---|---|
| Molecular weight (g/mol) | 1202 | Jamei et al., 2014 |
| log P | 2.96 | Jamei et al., 2014 |
| Compound type | Neutral | |
| B/P | 1.36 | Jamei et al., 2014 |
| $f_{u,p}$ | 0.0365 | Jamei et al., 2014 |
| Main plasma binding protein | Human serum albumin | |
| **Distribution** | | |
| Distribution model | Full PBK model | |
| $V_{ss}$ (L/kg) | 1.480513 | Predicted in Simcyp using Method 2<br>Rodgers et al., 2005; Rodgers and Rowland, 2006 |
| Predicted tissue:plasma partition coefficients | | |
| Adipose | 2.637 | |
| Bone | 2.532 | |
| Brain | 2.325 | |
| Gut | 1.927 | |
| Heart | 0.709 | |
| Kidney | 0.993 | |
| Liver | 1.571 | |
| Lung | 0.358 | |
| Muscle | 0.941 | |
| Skin | 1.162 | |
| Spleen | 1.067 | |
| Pancreas | 1.536 | |
| **Metabolism and excretion** | | |
| Enzyme | CYP3A4 | |
| Pathway | M1 (AM9) | |
| $V_{max}$ (pmol/min/pmol) | 1.7081 | Simcyp Compound File |
| $K_m$ (µM) | 3.02 | |

| Metabolism and excretion | | |
|---|---|---|
| Enzyme | CYP3A4 | |
| Pathway | M17 (AM1) | |
| $V_{max}$ (pmol/min/pmol) | 1.8395 | Simcyp Compound File |
| $K_m$ (µM) | 3.02 | |
| Enzyme | CYP3A4 | |
| Pathway | M21 (AM4N) | |
| $V_{max}$ (pmol/min/pmol) | 1.6424 | Simcyp Compound File |
| $K_m$ (µM) | 3.02 | |
| Enzyme | CYP3A5 | |
| Pathway | M17 (AM1) | |
| $V_{max}$ (pmol/min/pmol) | 9.061 | Simcyp Compound File |
| $K_m$ (µM) | 3.02 | |
| Active uptake into hepatocyte | 1.534 | Simcyp Compound File |
| $CL_{int}$ (bile) (µL/min/$10^6$ cells) | 0.45 | Simcyp Compound File |
| $CL_R$ (L/h) | 0.029 | Simcyp Compound File |

| Inhibition | | |
|---|---|---|
| Transporter | SLC10A1 (NTCP) | |
| Organ | Liver | |
| $K_i$ (µM) | 0.63 | Jamei et al., 2014 |
| Transporter | SLCO1B1 (OATP1B1) | |
| Organ | Liver | |
| $K_i$ (µM) | 0.014 | Jamei et al., 2014 |
| Transporter | SLCO1B3 (OATP1B3) | |
| Organ | Liver | |
| $K_i$ (µM) | 0.007 | Jamei et al., 2014 |
| Transporter | SLCO2B1 (OATP2B1) | |
| Organ | Liver | |
| $K_i$ (µM) | 13 | Vildhede et al., 2014 |
| Transporter | Canalicular Efflux (Liver) | |
| Organ | Liver | |
| $K_i$ (µM) | 0.07 | Wang et al., 2017 |

*Calculation of hepatic RSV concentrations*

In the bottom-up PBK model we published for RSV, the PerL model was utilized to account for the effect of numerous uptake transporters that mediate the distribution of RSV into the liver. The PerL within Simcyp has been described extensively previously (Jamei et al., 2014). Since the PerL model predicts the unbound IW and EW concentrations in the liver ($C_{u,IW}$ and $C_{u,EW}$) separately, there is a need to amalgamate the predicted concentrations from the PerL model into an overall hepatic concentration for comparison with the [$^{11}$C] PET imaging data. As a result, the overall hepatic concentration is:

$$Hepatic\ concentration = A_{liver} \div V_{liver} \quad (1)$$

where amount of RSV in the liver ($A_{liver}$) is calculated as:

$$A_{liver} = A_{IW} + A_{EW} + A_{VS} \quad (2)$$

$$A_{liver} = C_{IW} \times V_{IW} + C_{EW} \times V_{EW} + C_{B,VS} \times V_{VS} \quad (3)$$

$V_{IW}$, $V_{EW}$ and $V_{VS}$ represent the volume of the IW, EW and VS in the liver, and $C_{IW}$, $C_{EW}$ and $C_{B,VS}$ represent the concentration of the compound found within the IW, EW and blood of the VS in the liver. This equation can be simplified further into

$$A_{liver} = C_{IW} \times V_{IW} + C_{EW} \times V_{EW\text{-}eff} \quad (4)$$

where

$$V_{EW\text{-}eff} = V_{EW} + \frac{V_{VS}}{K_{EW:B}} \quad (5)$$

$V_{EW\text{-}eff}$ represents the effective EW liver volume, and $K_{EW:B}$ is a drug-dependent parameter that represents the ratio of $C_{EW}$ to $C_{B,VS}$ (Jamei et al., 2014). $V_{EW\text{-}eff}$ accounts for the distribution of chemical compounds found within the VS and EW of the liver (Jamei et al., 2014). Finally, to calculate the $A_{liver}$, we made use of the following equation

$$A_{liver} = \frac{C_{u,IW}}{f_{u,IW}} \times V_{IW} + \frac{C_{u,EW}}{f_{u,EW}} \times V_{EW\text{-}eff} \quad (6)$$

where

$$A_{liver} = \frac{C_{u,IW}}{f_{u,IW}} \times f_{IW} \times V_{liver} + \frac{C_{u,EW}}{f_{u,EW}} \times \left( f_{EW} + \frac{f_{VS}}{K_{EW:B}} \right) \times V_{liver} \quad (7)$$

$f_{u,EW}$ and $f_{u,IW}$ represent the fractions unbound of RSV in the EW and IW of the liver, which are predicted in Simcyp to be 0.187 and 0.967, respectively. $f_{IW}$, $f_{EW}$ and $f_{VS}$ represent the fractions of IW, EW and VS out of the total liver volume and are defined by Simcyp to be 0.835, 0.16 and 0.05, respectively. Hepatic concentrations from the PET imaging study were normalized against the mass of the liver and the intravenous dose of RSV given in kilobecquerels (kBq/g). For ease of comparison between simulated and measured values, the liver density value of 1.08 g/mL from Simcyp and the RSV dose given were applied to convert the hepatic concentrations measured in the imaging study to ng/mL.

All calculations were performed in Microsoft® Excel® for Office 365 (Microsoft, Redmond, WA, USA). Graphs were plotted and analyzed using GraphPad Prism 8 (GraphPad Software, La Jolla, CA, USA).

From a physiological perspective, the permeability-limited model does not fully account for the physiology of biliary excretion. Biliary excretion begins when hepatic canalicular efflux transporters in the hepatocyte excrete a compound via active transport. The excreted compound will enter the bile canaliculi, pass through the canals of Hering into the intrahepatic ducts, followed by consolidation into the common hepatic duct before it leaves the liver via the common bile duct and drains into the gall bladder (Boyer, 2013). We expect hepatic concentrations measured from PET images to be a composite of the concentrations found not only in the EW and IW space of liver cells but also within the bile canaliculi and possibly the intrahepatic ducts. It is mentioned by Billington et al. (2019) that the bile ducts were excluded from the PET scan images of the liver. However, this did not exclude RSV distributed into the bile canaliculi. As RSV is reliant on biliary excretion for its elimination, a substantial proportion of RSV hepatic concentration from the PET imaging study is expected to be found within the bile canaliculi during the initial phase of RSV disposition. Therefore, there was a need to adapt the PerL model parameters to account for distribution into the bile canaliculi. We employed a workaround that would account for the bile canaliculi concentration by removing the biliary excretion component of RSV via changing the liver canalicular efflux intrinsic clearance ($CL_{int}$) input value to 0. This had the effect of combining RSV that would normally be found in the bile canaliculi with RSV found within the IW and EW space, thus allowing us to account for the fraction of RSV that resides in the bile canaliculi in the initial phase of its disposition.

## 2.2 Model validation

*Independent simulation of plasma concentrations of RSV and CsA*
Validation of the PBK models of RSV and CsA were conducted by performing simulations that matched the design of the PET imaging clinical study. Using the Simcyp Healthy Volunteers population database, simulations for two separate trials were performed for a 0.91 µg IV bolus dose of RSV and 2.5 mg/kg/h IV infusion of CsA. Refer to Table 3 for details of the population characteristics. As a range of doses (0.91–2.57 µg, equivalent to 309–689 MBq) were administered to the subjects in the PET imaging study, the lowest dose of RSV 0.91 µg was chosen. Simulated plasma concentrations were compared against the plasma concentrations of RSV and CsA from the PET imaging study extracted using WebPlotDigitizer (San Francisco, California, USA). To validate the RSV PBK model, a two-fold criterion was applied to compare the predicted against observed biokinetic parameters including maximum plasma concentration ($C_{max}$) and area under the plasma concentration-time profile ($AUC_{0\text{-}30min}$). For the CsA model, visual inspection of the predicted against observed plasma-concentration time profile was used for validation because biokinetic parameters of CsA were not reported by Billington et al. (2019).

*Simulating plasma concentrations of RSV post-DDI with CsA*
A second level of validation was performed to ascertain that our PBK models were able to predict the DDI between RSV and CsA. Using the same population database and trial design, a CsA 2.5 mg/kg/h IV infusion over 2 h followed by a RSV 0.91 µg IV bolus dose 45 min after the initiation of the CsA IV infusion was simulated. Similarly, a two-fold criterion was applied to compare the predicted against observed biokinetic parameters, $C_{max}$, $AUC_{0\text{-}30min}$ and $T_{max}$ for RSV after the DDI with CsA. $C_{max}$ and $AUC_{0\text{-}30min}$ ratios were evaluated using the quotient of the values after and before DDI.

## 2.3 Model application

*Simulating hepatic concentrations of RSV pre- and post-DDI with CsA*
Using the same trial design mentioned, we applied the bottom-up RSV PBK model to simulate RSV hepatic concentrations after a 0.91 µg RSV IV bolus dose. As mentioned previously, during initial simulations of the unchanged RSV PBK model, predictions of hepatic concentrations were suboptimal. Modification of the PerL model biliary excretion parameter was performed to account for distribution of RSV within the bile canaliculi. Comparison of the simulations before and after this modification was done to understand the impact of this modification. Furthermore, as PET imaging scans are unable to differentiate the parent [$^{11}$C] RSV and its metabolite, metabolism of RSV in the PBK model was switched off to recapitulate this effect when predicting RSV hepatic concentrations. After the above optimization of the PBK model of RSV to predict hepatic concentrations, we proceeded to predict the effect of a DDI with CsA on RSV hepatic concentrations. Comparison of the simulated maximum hepatic concentration ($C_{max,liver}$), area under the hepatic concentration-time profile ($AUC_{0\text{-}30min,liver}$), time needed to reach $C_{max,liver}$ ($T_{max,liver}$), and $AUC_{0\text{-}30min,liver}/AUC_{0\text{-}30min}$ ratio against the observed data was

**Tab. 3: Details of the simulated clinical trial population characteristics**

| Simulation trial | Number of trials | Number of participants | Proportion of females | Age range (years) | Reference |
|---|---|---|---|---|---|
| PET imaging study | 10 | 10 | 0.66 | 24-28 | Billington et al., 2019 |
| Predicting hepatic $K_{p,liver}$ and $K_{p,uu,liver}$ | 10 | 10 | 0.5 | 25-55 | |
| PK/PD correlation | 10 | 10 | 0.5 | 25-55 | |

performed. For the DDI trial, ratios of $C_{max,liver}$, $AUC_{0\text{-}30min,liver}$ and $AUC_{0\text{-}30min,liver}/AUC_{0\text{-}30min}$ post-DDI to pre-DDI were evaluated.

*Comparison of hepatic tissue concentrations predicted using a permeability-limited versus perfusion-limited approach*

To further evaluate the performance of a permeability-limited approach in predicting the transporter-mediated distribution of RSV into the liver, a simulation was performed to calculate the liver tissue:plasma partition coefficient ($K_{p,liver}$) and $K_{p,uu,liver}$ of RSV using the PerL model. Using the Simcyp Healthy Volunteer population database, a 1.0 mg/kg/h IV infusion was administered for 96 h to obtain equilibrium concentrations of RSV in the plasma and liver (Tab. 3). Subsequently, the ratio of $AUC_{0\text{-}96h,liver}$ to $AUC_{0\text{-}96h}$ was calculated to obtain $K_{p,liver}$. To determine $K_{p,uu,liver}$, the ratio of unbound $AUC_{0\text{-}96h,liver}$ of the IW component ($AUC_{0\text{-}96,liver,IW}$) to unbound $AUC_{0\text{-}96h}$ was calculated, where unbound $AUC_{0\text{-}96h,liver,IW}$ was obtained from the product of $f_{u,IW}$ and $AUC_{0\text{-}96,liver,IW}$, while unbound $AUC_{0\text{-}96h}$ was obtained from the product of $f_{u,p}$ and $AUC_{0\text{-}96}$.

*Evaluating the PK/PD correlation of rosuvastatin*

The RSV PBPK model was utilized to perform a PK/PD correlation of RSV with the predicted plasma and hepatic concentration-time profile. The lowest clinically used oral dose of 5 mg repeated once daily over a duration of 7 days was simulated using the Simcyp Healthy Volunteer population database (Tab. 3). The predicted RSV $C_{u,IW}$, plasma concentration ($C_p$) and unbound $C_p$ ($C_{u,p}$) were compared against the reported 50% inhibitory concentration ($IC_{50}$) against HMG-CoA reductase (McTaggart et al., 2001) to assess whether our PBPK model was able to replicate the clinical efficacy observed at this dose.

*Sensitivity analysis of the input parameters within the PerL model*

Parameter sensitivity analyses were performed using the local sensitivity analysis function available within Simcyp. The objectives of our sensitivity analysis were: (1) identify key model input parameters that influenced the predicted plasma and/or hepatic biokinetic parameters, and (2) investigate our hypothesis that modification of the PerL model by removing the biliary excretion component is necessary to recapitulate the RSV hepatic concentrations from the PET imaging study. Model input parameters for the PerL model were increased and decreased by 2, 4, 8 and 16-fold. The corresponding change in output parameters such as $C_{max}$, $AUC_{0\text{-}30min}$ pre-and post-DDI were investigated. As the local sensitivity analysis function only outputs the variation in $C_{u,IW}$ pre-DDI, both $C_{max,IW}$ and $AUC_{0\text{-}30min,IW}$ were regarded as a suitable surrogate measure of the hepatic biokinetic parameters. We were unable to investigate the impact of varying the model input parameters for hepatic biokinetic parameters post-DDI due to limitations in the local sensitivity analysis function.

## 3 Results

### 3.1 Model validation of RSV and CsA

Results of our simulations for the 0.91 µg IV bolus dose of RSV and the 2.5 mg/kg/h IV infusion of CsA demonstrate that the independent models accurately predicted the clinical results of the PET imaging study. The plasma concentration-time profile for the RSV and CsA simulations are presented in Figures 2 and 3, respectively. It should be noted that RSV plasma concentrations from only a single subject from the PET imaging study were available for comparison. Predicted $AUC_{0\text{-}30min}$ and $C_{max}$ of the whole study cohort for RSV (Tab. 4) were within 1.5-fold of the observed clinical data (fold difference of 0.879 and 1.279). Biokinetic parameters for CsA were not reported in the PET imaging study and are not assessed here.

After validating the RSV and CsA models independently, we moved on to validate the DDI model between RSV and CsA. The predicted plasma concentration-time profiles before and after the DDI are presented in Figure 4. Similarly, only clinical data for the RSV plasma concentration-time profile of a single sub-

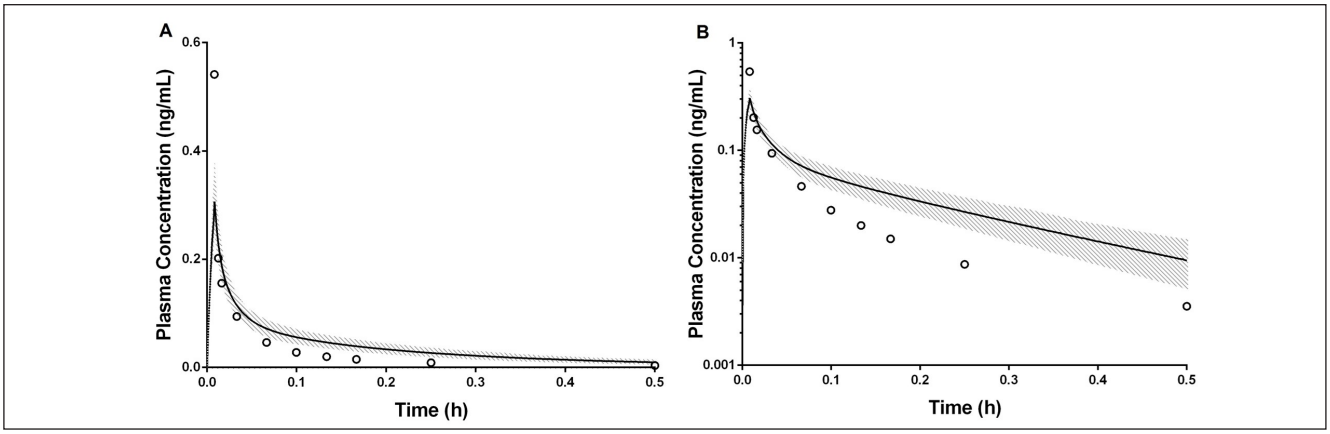


**Fig. 2: RSV plasma concentration-time profile for simulations of 0.91 µg IV bolus dose of RSV in both linear (A) and $log_{10}$ y-axis scale (B)**

The black circles represent the RSV clinical data from the PET imaging study; the solid black lines represent the simulated mean RSV plasma concentrations with the 95th and 5th percentile bounded by the grey shaded area.

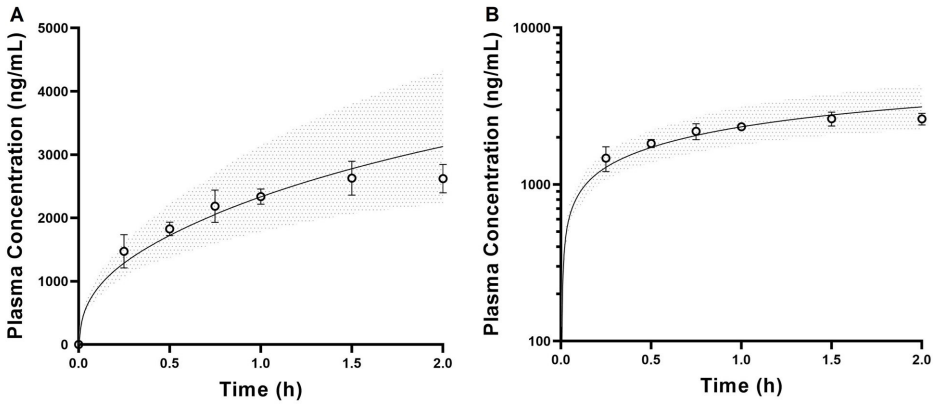


**Fig. 3: CsA plasma concentration-time profile for simulations of 2.5 mg/kg/h IV infusion of CsA in both linear (A) and $log_{10}$ y-axis scale (B)**

The black circles represent the CsA clinical data from the PET imaging study with the standard deviation represented by the error bars; the solid black lines represent the simulated mean CsA plasma concentrations with the 95$^{th}$ and 5$^{th}$ percentile bounded by the grey shaded area.

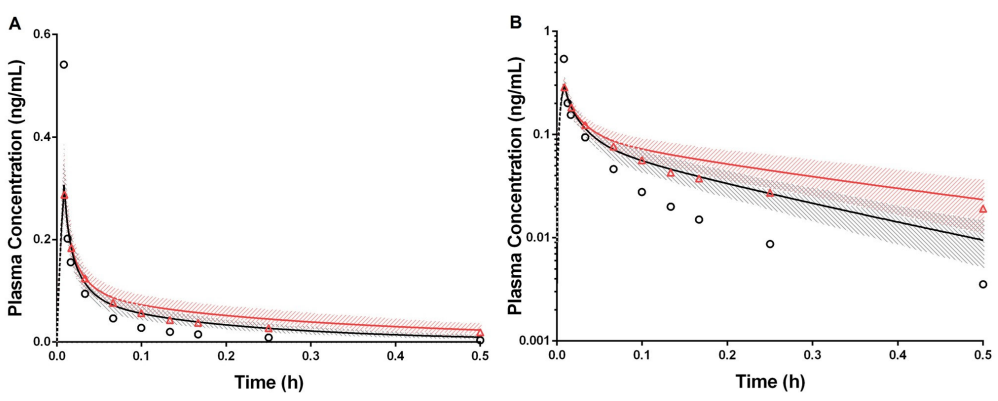


**Fig. 4: RSV plasma concentration-time profile of the simulated drug-drug interaction between a 0.91 *µ*g IV bolus dose of RSV and 2.5 mg/kg/h IV infusion of CsA in both linear (A) and $log_{10}$ y-axis scale (B)**

The black circles and red triangles represent the RSV clinical data before and after the DDI with CsA. The solid black and red lines represent the simulated mean RSV plasma concentrations before and after the drug-drug interaction with the 95$^{th}$ and 5$^{th}$ percentile bounded by the grey and red shaded areas, respectively.

**Tab. 4: Simulated versus observed plasma biokinetic parameters for RSV pre- and post-DDI with CsA**

| Biokinetic parameter | Observed | Predicted | Fold difference |
|---|---|---|---|
| Plasma | Mean (SD) | Geometric mean (5$^{th}$ - 95$^{th}$ percentile) | Predicted/observed |
| **Before DDI** | | | |
| $C_{max}$ (ng/mL) | 0.346 (0.100) | 0.304 (0.247-0.390) | 0.879 |
| $AUC_{0\text{-}30min}$ (ng/mL*h) | 0.016 (0.002) | 0.021 (0.017-0.026) | 1.279 |
| **After DDI** | | | |
| $C_{max}$ (ng/mL) | 0.319 (0.100) | 0.304 (0.248-0.390) | 0.956 |
| $AUC_{0\text{-}30min}$ (ng/mL*h) | 0.023 (0.002) | 0.028 (0.022-0.038) | 1.209 |
| $C_{max}$ ratio | 0.921 | 1.002 | 1.088 |
| $AUC_{0\text{-}30min}$ ratio | 1.453 | 1.372 | 0.945 |

ject was available for comparison. After the DDI with CsA, the plasma concentrations of RSV increased. The predicted RSV $AUC_{0\text{-}30min}$ increased from 0.021 to 0.028 ng/mL with an $AUC_{0\text{-}30min}$ ratio of 1.372, whereas the predicted $C_{max}$ remained unchanged at 0.304 ng/mL with a ratio of 1.002. When compared against the observed data, predicted $AUC_{0\text{-}30min}$ and $C_{max}$ after the DDI with CsA were within 1.5-fold of the observed data (Tab. 4). Importantly, the predicted $AUC_{0\text{-}30min}$ and $C_{max}$ ratios exhibited a fold difference of 1.088 and 0.945 when compared against the observed data. The model was able to recapitulate the extent of increase in plasma concentrations and $AUC_{0\text{-}30min}$ as well as the unchanged $C_{max}$ of RSV after the DDI with CsA.

### 3.2 Simulations of hepatic concentrations of RSV

Results for the simulations of RSV hepatic concentrations with and without modifying biliary clearance to account for distribution into the bile canaliculi of the liver are illustrated in Figure 5. The predicted biokinetic parameters versus the observed values are found in Table 5. When the fraction distributed into the bile canaliculi was not accounted for, simulations for RSV hepatic concentrations predicted a gradual decrease in hepatic concentrations after 0.05 h. In this scenario, the fold difference of $C_{max,liver}$, $AUC_{0\text{-}30min,liver}$ and $T_{max}$ were outside the two-fold criterion, and the model was unable to recapitulate the observed increase in RSV concentrations within the liver. $C_{max,liver}$

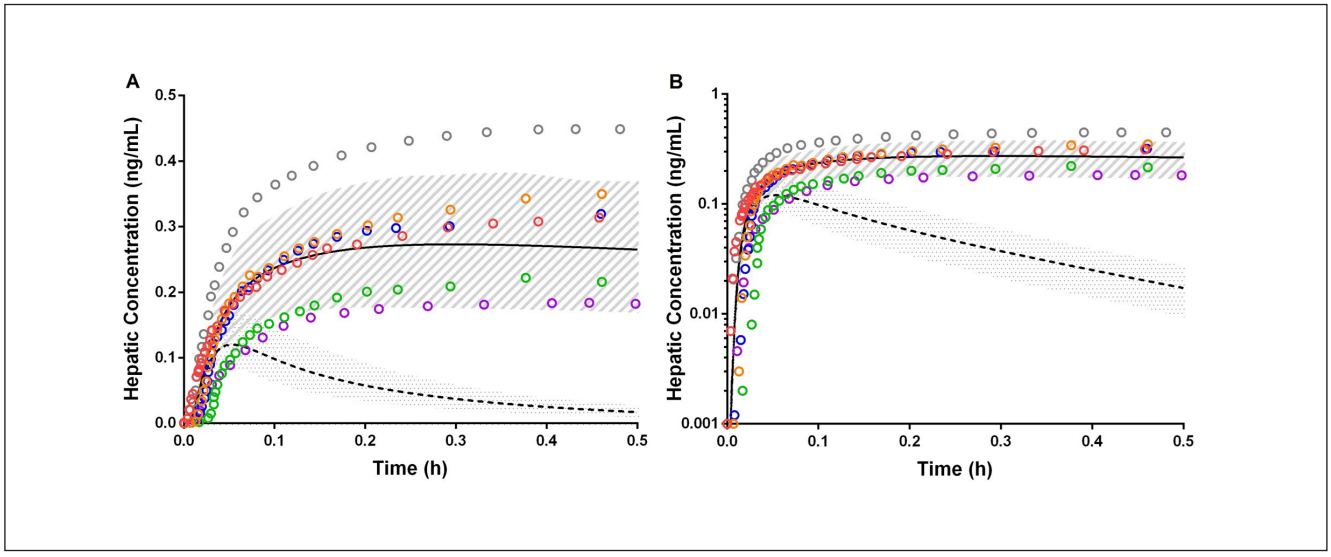


**Fig. 5: RSV hepatic concentration-time profile after a 0.91 $\mu$g IV bolus dose of RSV with and without accounting for distribution within the bile canaliculi in both linear (A) and $log_{10}$ y-axis scale (B)**

The circles represent the observed RSV hepatic concentrations for 6 individual subjects, each with a different color. The solid and dashed black lines represent the simulated hepatic concentrations with and without accounting for distribution within the bile canaliculi, and the grey shaded area bounds the 95$^{th}$ and 5$^{th}$ percentile of each simulation.

**Tab. 5: Simulated versus observed hepatic biokinetic parameters for the simulation of RSV hepatic concentrations with and without accounting for the distribution of RSV into the bile canaliculi**

| Biokinetic parameter | Observed | Predicted | Fold difference |
|---|---|---|---|
| Hepatic | Mean (SD) | Geometric mean (5$^{th}$ - 95$^{th}$ percentile) | Predicted/observed |
| **Before accounting for distribution into bile canaliculi** | | | |
| $C_{max,liver}$ (ng/mL) | 0.277 (0.087) | 0.120 (0.083-0.172) | 0.434 |
| $AUC_{0\text{-}30min,liver}$ (ng/mL*h) | 0.129 (0.042) | 0.026 (0.016-0.040) | 0.206 |
| $T_{max,liver}$ (h) | 0.432 (0.037) | 0.053 (0.061-0.058) | 0.123 |
| **After accounting for distribution into bile canaliculi** | | | |
| $C_{max,liver}$ (ng/mL) | 0.277 (0.087) | 0.273 (0.177-0.383) | 0.986 |
| $AUC_{0\text{-}30min,liver}$ (ng/mL*h) | 0.129 (0.042) | 0.122 (0.080-0.169) | 0.951 |
| $T_{max,liver}$ (h) | 0.432 (0.037) | 0.296 (0.209-0.368) | 0.686 |

and $AUC_{0\text{-}30min,liver}$ were underpredicted with a fold difference of 0.434 and 0.206. When the distribution of RSV into the bile canaliculi was included in the calculation of hepatic concentrations, the newly predicted $C_{max,liver}$ (0.273 ng/mL) and $AUC_{0\text{-}30min,liver}$ (0.122 ng/mL*h) closely matched the observed values (0.277 ng/mL and 0.129 ng/mL*h) with a fold difference of 0.986 and 0.951, respectively. Upon comparing the ratio of $AUC_{0\text{-}30min,liver}/AUC_{0\text{-}30min}$, blood, the predicted value of 9.514 closely matched the observed value of 12.66 ± 5.83 (mean ± SD) in the PET imaging study, with a fold difference of 0.752. The model was also able to recapitulate the observed plateau of RSV hepatic concentrations during the first 30 min after the IV bolus dose.

### 3.3 Simulations of hepatic concentrations RSV post-DDI with CsA

Having demonstrated the ability of our PBK model to predict RSV hepatic concentration-time profiles, we proceeded to simulate the effect of a DDI between RSV and CsA on the predicted RSV hepatic profiles. Our model was able to recapitulate the observed decrease in hepatic concentrations of RSV after a DDI with CsA (Fig. 6). After the DDI, predicted $C_{max,liver}$ decreased from 0.273 ng/mL to 0.175 ng/mL with a $C_{max,liver}$ ratio of 0.640 and predicted $AUC_{0\text{-}30min,liver}$ decreased from 0.122 ng/mL*h to 0.079 ng/mL*h with a $AUC_{0\text{-}30min,liver}$ ratio of 0.645 (Tab. 6). Compared to the observed $C_{max,liver}$ (0.242 ng/mL) and $AUC_{0\text{-}30min,liver}$ (0.108 ng/mL*h) after the DDI with CsA, the predicted parameters were slightly underpredicted but still fell within 1.5-fold (0.721 and 0.733) of the observed value, whereas the predicted $C_{max,liver}$ and $AUC_{0\text{-}30min,liver}$ ratio was 0.732 and 0.771-fold the observed values, respectively. While this demonstrates a slight overprediction of the impact of a DDI with CsA on RSV hepatic concentrations, the predicted biokinetic parameters were within our two-fold acceptance criteria.

### 3.4 Predictions of liver tissue:plasma concentration ratio and PK/PD correlation of rosuvastatin

After a 1.0 mg/kg/h IV infusion administered for 96 hours, the predicted mean $K_{p,liver}$ and $K_{p,uu,liver}$ were 1.13 and 11.70 when the original RSV model (Chan et al., 2019) was used. This represents a significant accumulation of the unbound drug in the liver versus the plasma. Similarly, when the lowest clinical dose of RSV was simulated, the predicted RSV $C_{u,IW}$ remained above the $IC_{50}$ value of 2.6 ng/mL (McTaggart et al., 2001) for the majority of the dosing interval (Fig. 7). In contrast, the predicted $C_p$ remained below the $IC_{50}$ threshold for most of the dosing interval, and the predicted $C_{u,p}$ fell below the $IC_{50}$ threshold for the entire dosing interval. Correlation between the PK/PD of RSV was best predicted when the predicted $C_{u,IW}$ was used to compare against the $IC_{50}$ threshold.

### 3.5 Sensitivity analyses

Upon varying the drug input parameters of the PerL model by 2- to 16-fold of their original value, the sensitivity analysis revealed that the plasma biokinetic parameters ($C_{max}$ and $AUC_{0\text{-}30min}$ before and after the DDI) were insensitive to changes in the input parameters. In contrast, the predicted $C_{max,IW}$ was sensitive to changes in the OATP1B1 maximal transport rate ($J_{max}$) and passive diffusion clearance ($CL_{pd}$) input parameters (Fig. 8A). In particular, when $CL_{pd}$ increased by 16-fold, the resultant $C_{max,IW}$ decreased by 4-fold. A similar effect was observed for $AUC_{0\text{-}30min,IW}$.

To investigate if removing the biliary excretion component was necessary to recapitulate the hepatic concentrations from the PET imaging study, we utilized the unchanged PBK model of RSV and varied the input parameters of the PerL model by 2- to 16-fold. Other than the canalicular efflux $CL_{int}$ input parameter, changing the input parameters of the PerL model led to minimal change in the output $C_{IW}$. The model was sensitive only to changes in the canalicular efflux $CL_{int}$ (Fig. 8B). However, de-

**Tab. 6: Simulated versus observed hepatic biokinetic parameters for the DDI between RSV and CsA**

| Biokinetic parameter | Observed | Predicted | Fold difference |
|---|---|---|---|
| **Hepatic** | **Mean (SD)** | **Geometric mean ($5^{th}$ - $95^{th}$ percentile)** | **Predicted/observed** |
| **Before DDI** | | | |
| $C_{max,liver}$ (ng/mL) | 0.277 (0.087) | 0.273 (0.177-0.383) | 0.986 |
| $AUC_{0\text{-}30min,liver}$ (ng/mL*h) | 0.129 (0.042) | 0.122 (0.080-0.169) | 0.951 |
| $T_{max,liver}$ (h) | 0.432 (0.037) | 0.296 (0.209-0.368) | 0.686 |
| **After DDI** | | | |
| $C_{max,liver}$ (ng/mL) | 0.242 (0.087) | 0.175 (0.110-0.244) | 0.721 |
| $AUC_{0\text{-}30min,liver}$ (ng/mL*h) | 0.108 (0.042) | 0.079 (0.047-0.111) | 0.733 |
| $T_{max,liver}$ (h) | 0.450 (0.022) | 0.178 (0.104-0.265) | 0.395 |
| $C_{max,liver}$ ratio | 0.875 | 0.640 | 0.732 |
| $AUC_{0\text{-}30min,liver}$ ratio | 0.836 | 0.645 | 0.771 |

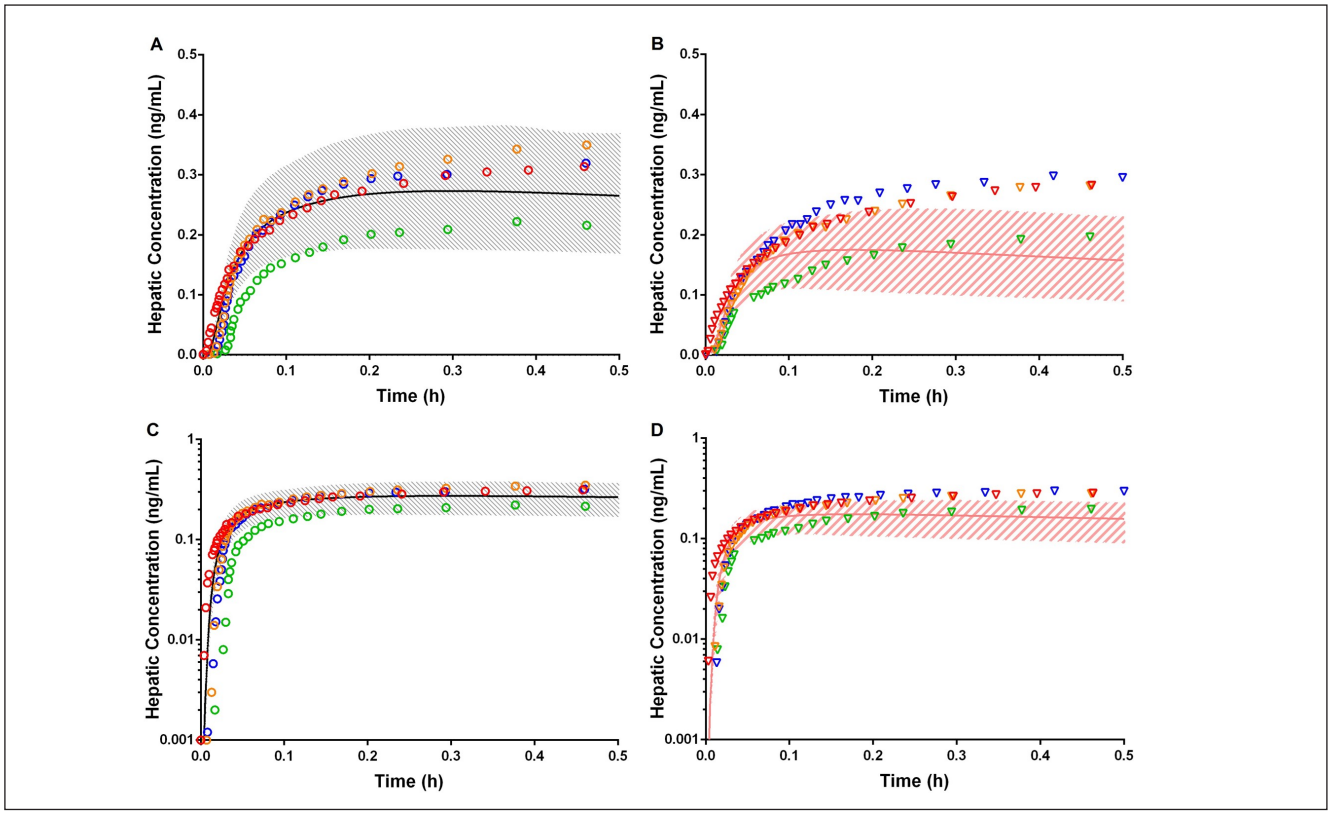


**Fig. 6: RSV hepatic concentration-time profile before (A, C) and after (B, D) a simulated drug-drug interaction between a 0.91 *μ*g IV bolus dose of RSV and 2.5 mg/kg/h IV infusion of CsA in both linear (A, B) and $log_{10}$ y-axis scale (C, D)**
The circles and triangles represent the observed RSV hepatic concentrations before and after the drug-drug interaction, respectively for 4 individual subjects. Each subject is represented by circles and triangles of the same color. The solid black and red lines represent the simulated RSV hepatic concentrations before and after the drug-drug interaction, and the grey and red shaded areas bound the 95$^{th}$ and 5$^{th}$ percentile of each simulation.

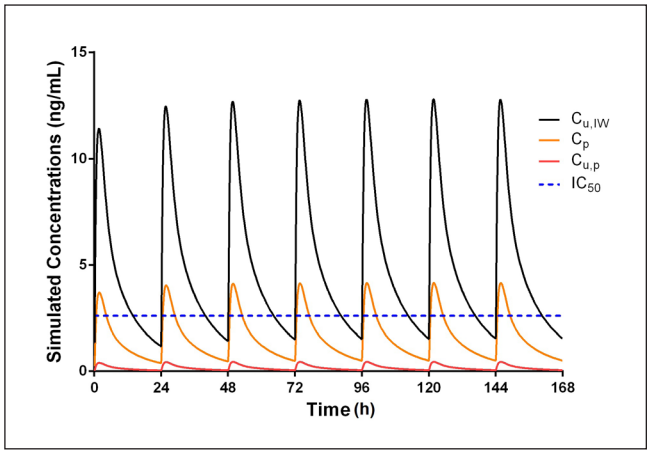


**Fig. 7: RSV unbound intracellular hepatic ($C_{u,IW}$), total plasma ($C_p$) and unbound plasma ($C_{u,p}$) concentration-time profile after a repeated once daily oral dose of 5 mg RSV for 7 days**
The solid black, orange and red lines represent the simulated RSV $C_{u,IW}$, $C_p$ and $C_{u,p}$. The dashed blue line represents the $IC_{50}$ of RSV against HMG-CoA reductase.

creasing the $CL_{int}$ 16-fold was still insufficient to reach the predicted $C_{IW}$ obtained with the modified PBK model (Fig. 8C).

## 4 Discussion

In this study, we hypothesized that bottom-up PBK modelling would be able to recapitulate the hepatic concentrations of RSV as well as accurately predict the impact of CsA on the hepatic concentrations of RSV, using the recently published PET imaging study by Billington et al. (2019) to validate our simulations. In doing so, we aimed to build further understanding of the ability of bottom-up PBK modelling to predict tissue concentrations. We utilized the bottom-up PBK model of RSV that we published previously and adapted a CsA PBK model from the Simcyp compound file library with modifications to the inhibitory constants. By successfully recapitulating the plasma biokinetics of a RSV IV bolus dose prospectively, before and after a DDI with CsA, we demonstrated the robustness of PBK modelling in predicting the impact of a DDI on plasma concentrations.

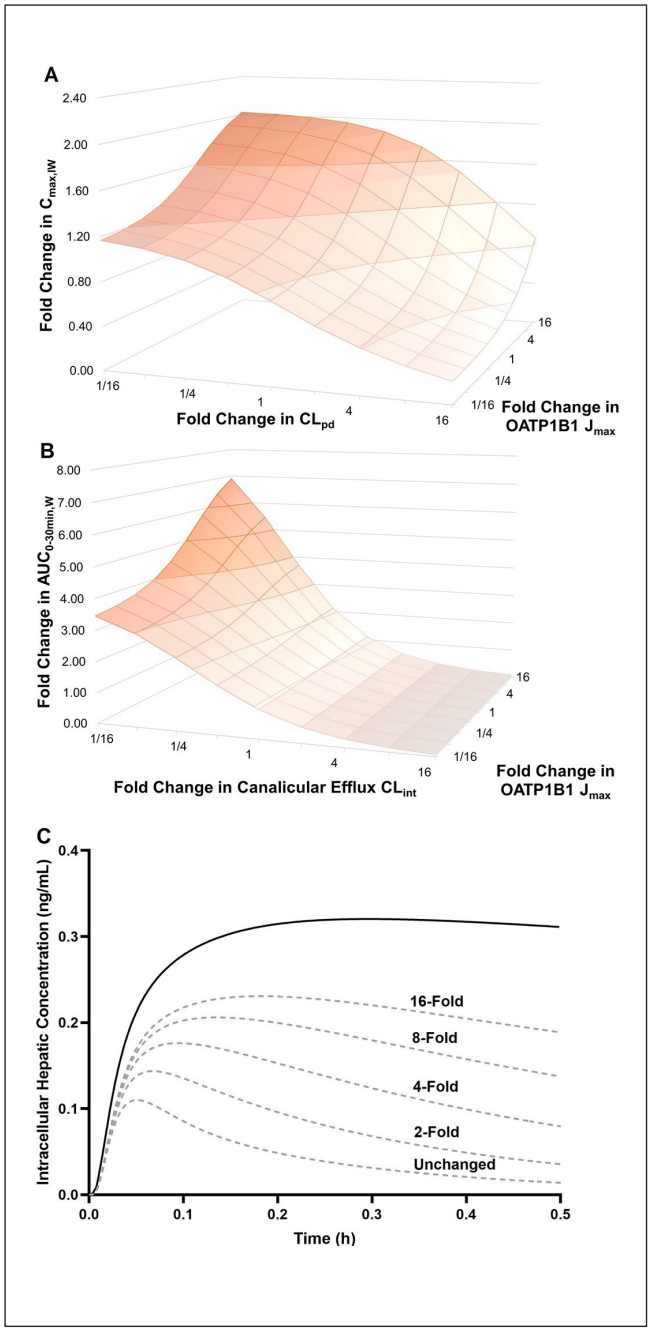


**Fig. 8: Quantitative effect of the local sensitivity analysis on the predicted hepatic biokinetic parameters**

(A) Fold change in $C_{max,IW}$ with respect to changes in the OATP1B1 $J_{max}$ and $CL_{pd}$ input parameters when the modified PBK model was utilized. (B) Fold change in $AUC_{0-30min,IW}$ with respect to changes in the OATP1B1 $J_{max}$ and canalicular efflux $CL_{int}$ input parameters when the unmodified PBK model was utilized. (C) Variation in the predicted RSV intracellular hepatic concentration-time profile ($C_{IW}$) where the dashed grey line represents the effect of decreasing canalicular efflux $CL_{int}$ by 2-, 4-, 8- and 16-fold; the black line represents the predicted $C_{IW}$ using the modified PBK model.

Due to its poor passive permeability, the uptake of RSV into the liver is permeability-limited and mediated by numerous hepatic transporters such as OATP1B1, OATP1B3, OATP2B1 and NTCP. As these active transporters facilitate the uptake transport of unbound drugs against the concentration gradient, this would lead to an accumulation of unbound drug in the intracellular space of the liver. Moreover, as the rate of passive permeability is much lower than the rate of active uptake for RSV, the accumulated intracellular unbound drug would not be able to equilibrate with the vascular space or extracellular water. Hence, this leads to asymmetrical unbound RSV concentrations between the liver and plasma at steady state (Zhang et al., 2019b). This phenomenon is recapitulated in our predicted $K_{p,uu,liver}$ values of 11.70. These values are comparable to the $K_{p,uu,liver}$ values of 11.6 and 6.36 measured using suspended human hepatocytes (Yoshikado et al., 2017). Other reported values for $K_{p,uu,liver}$ include 35 and 57, measured using suspended rat hepatocytes and in an *in vivo* rat study (Riccardi et al., 2017). Collectively, these indicate that a permeability-limited approach can recapitulate the liver accumulation of RSV. Furthermore, by utilizing the PerL model, our unchanged PBK model of RSV was able to replicate the observed clinical efficacy of the lowest clinical dose of RSV (5 mg daily dosing). This is demonstrated by the predicted $C_{u,IW}$ remaining above the $IC_{50}$ value for most of the dosing interval of 24 hours. This highlights the importance of assessing tissue concentration, which represents the location of the biological target. Plasma concentrations, which can be distant from the site of action, may provide misleading information as demonstrated by our predictions of $C_p$ and $C_{u,p}$ falling below the $IC_{50}$ threshold for most if not the entire dosing interval. Utilizing $C_{u,IW}$ provided the most accurate PK/PD correlation for the lowest clinically used dose of RSV.

While OATP1B1, OATP1B3, OATP2B1 and NTCP mediate the active uptake of RSV into the liver, BCRP and possibly P-gp actively excrete RSV into the bile canaliculi, facilitating its elimination into bile. CsA being a potent inhibitor of OATP1B1, OATP1B3 and BCRP would lead to an increase in plasma concentrations of RSV, as the hepatic uptake and excretion of RSV is limited and clearance is reduced. This DDI has been observed not only in the PET imaging study but also clinically in heart transplant patients (Simonson et al., 2004). A dose reduction of RSV when co-administering RSV with CsA is recommended in the Crestor® product label (Astra Zeneca, 2003). While the change in plasma concentrations after a DDI with CsA is clear, it is crucial to understand how a DDI with CsA will impact the unbound tissue concentrations of RSV. The change in unbound tissue concentrations, rather than the total or unbound plasma concentration (Chu et al., 2013), is the key determinant of the efficacy and toxicity of RSV. As the $K_{p,uu,liver}$ of RSV is much greater than 1, the unbound plasma concentration of RSV is not a reliable surrogate measure for the unbound hepatic concentration of RSV. In other words, an increase in unbound plasma concentrations of RSV after a DDI with CsA may not necessarily represent an increase in unbound hepatic concentration of RSV. This is because CsA inhibits both the hepatic uptake and biliary efflux of RSV, rendering the change in hepatic concentrations of RSV dependent on the relative magnitudes of inhibition of hepatic uptake (liver input) and biliary efflux (liver

output). In the PET imaging study, a decrease in overall hepatic RSV concentrations was observed, and we recapitulated the same results with our PBK model predictions after we modified the biliary excretion input parameter to account for distribution within the bile ducts. The latter point highlights a limitation of *in vivo* tissue imaging, which lacks sufficient resolution to further discriminate between RSV found within tissue extracellular (such as bile canaliculi) and intracellular spaces (Guo et al., 2018).

In addition to the above, the PerL model is constructed such that any biliary excreted compound is transferred from the intracellular liver into the enterohepatic compartment immediately, and the predicted liver concentrations will not account for the presence of RSV within the bile canaliculi. Hence, a discrepancy between model outputs and observed data could arise from (1) an inability of the imaging approach to discriminate between biliary and intracellular RSV content, and/or (2) the absence of a bile canalicular compartment within the PerL model. To resolve this conundrum, we modified the input parameters of the PerL model by switching off biliary excretion in order to retain RSV within the IW and EW liver compartments. We acknowledge that this may be an unconventional approach, as this results in the inclusion of not just canalicular RSV but also of RSV accumulated in the gallbladder. In the analysis of [$^{11}$C]RSV concentrations, Billington et al. (2019) excluded the gallbladder content (observed as a bright spot within the PET image), which indicates our approach may overestimate RSV levels. Nevertheless, we judged that our approach is an acceptable compromise for the following reasons: Firstly, the fasting volume of the gallbladder is around 21.9 mL (Loreno et al., 2009), while the volume of the liver in a healthy adult reported in Simcyp is roughly 1650 mL. This suggests that the RSV content within the gallbladder is a small fraction of that found within total liver spaces. Secondly, the observed concentration of [$^{11}$C]RSV remained constant throughout the dosing interval, which could be recapitulated by the simulation only when biliary excretion was set to zero, while a rapid decline is observed with biliary excretion activated. This is supported by our sensitivity analysis, which revealed that the predicted hepatic concentrations were sensitive only to changes in the biliary excretion input parameter. In general, changes in hepatic concentrations required exaggerated changes in PerL input parameters that are unrealistic, given that these are *in vitro* measurements and not values predicted using *in silico* methods where a greater degree of variability can be expected. In other words, this is consistent with our postulation that the majority of RSV is still found within hepatocytes, interstitial spaces or bile canaliculi in the first 30 minutes, and modification of the PerL model was necessary in order to recapitulate this observation. This point illustrates how modelling can discern a mechanistic explanation for observed data trends. Finally, we were able to recapitulate the observed [$^{11}$C]RSV hepatic profiles in two different regimens, i.e., RSV alone and with a CsA-mediated DDI, demonstrating the robustness of our approach under varying exposure regimens.

In addition to the above, our study has other limitations. For example, we were unable to account for the inhibition of biliary efflux of RSV by CsA, as we utilized an overall intrinsic biliary clearance *in vitro* parameter for RSV. However, we believe that the impact of this limitation is minimal during the first 30 minutes after the administration of RSV since the mean terminal elimination half-life of RSV is 20.3 - 31.3 hours (Martin et al., 2002, 2003). To recapitulate the whole liver concentrations obtained from the PET imaging study, a custom permeability hepatic model can be constructed to include the distribution within the bile canaliculi as well as the canalicular bile flow. As doing so would require additional model construction and validation, we believe that the use of our previously validated PBK model of RSV to predict whole liver hepatic concentrations is sufficient to demonstrate the ability of PBK modelling to predict tissue concentrations.

The value of this work lies in illustrating an approach by which PBK modelling, when parameterized by relevant *in vitro* data pertaining to the tissue uptake and efflux of xenobiotics, is able to quantitatively describe local tissue biokinetics in humans. While this case study uses RSV as a model compound, the approach is generalizable to (1) other chemicals and (2) other organs where transporters influence tissue concentrations. This is useful for the following reasons: Firstly, animals are still the go-to model when assessments of tissue concentrations are required; however, we show here that modelling and simulation is able to accurately reproduce the time-course of tissue levels within the human liver. We anticipate that this will spur a shift towards greater adoption of PBK modelling to reduce/replace the use of animals in obtaining tissue concentrations. Secondly, the approach we have demonstrated is not bespoke or applicable only to RSV, but to any chemical that utilizes transporters for tissue penetration and clearance. The transporters studied here are well-known xenobiotic transporters that transport many exogenous organic acids. Once the relevant kinetics of uptake and efflux are characterized for a particular chemical, it is straightforward to parameterize the PBK model and estimate human tissue concentrations. Finally, this approach can be adapted for other organs with high transporter expression, such as the kidneys, provided the unique physiology of these organs is carefully accounted for in the model.

In summary, we hope that our study will build further confidence in the use of PBK modelling to recover tissue concentrations of xenobiotics and encourage broader exploration and adoption of this methodology in place of animal toxicokinetic studies for the risk assessment of xenobiotics (Punt et al., 2017). We anticipate that PBK modelling can be applied in parallel with chemical discovery and development, where it will form part of the decision-making process when deciding whether a novel compound moves on to the next phase of development. To achieve this, further development and verification of PBK models for a broader range of xenobiotic compounds must be performed alongside robust measurements of *in vivo* human tissue biokinetic data for the same compound coupled with the consultancy of regulatory authorities (Paini et al., 2019). Eventually, this will help refine the design of *in vivo* biokinetic studies and thus reduce the number of animals needed for efficacy and safety testing of chemicals.

## 5 Conclusion

In conclusion, our study has demonstrated the ability of bottom-up PBK modelling to accurately predict the plasma and liver concentrations of RSV before and after a DDI with CsA. We

are unaware of other comparable studies that have demonstrated the ability of a well-parameterized bottom-up PBK approach to accurately predict human tissue chemical concentrations. Importantly, our work also demonstrates that it is possible to predict the impact of co-administration of interacting mixtures of chemicals, provided the points of interaction are well-characterized. We hope that our study will encourage future application of bottom-up PBK modelling in predicting both plasma and tissue concentrations during the development and risk assessment of novel chemicals in place of animal biokinetic testing. Our study has also highlighted several limitations of using PET imaging studies to predict hepatic concentrations as well as the limitation of using the PerL model to recapitulate the hepatic concentrations obtained from such PET imaging studies. Future studies should be conducted to further understand the relevance of PET imaging in obtaining tissue concentrations as well as to improve the PerL model by including a physiologically-relevant bile canaliculi compartment. Our work highlights that mechanistic PBK modelling approaches can accurately predict tissue concentrations of chemicals, provided sufficient *in vitro* data is available to parameterize these models. Furthermore, utilizing PBK model predicted tissue concentrations will enable better PK/PD correlation versus the use of plasma concentration. We envision that our work will spur industry to characterize their chemicals with appropriate *in vitro* ADME assays and utilize PBK modelling to obtain critical *in vivo* human tissue biokinetic predictions and perform pharmacodynamic/toxicodynamic correlations.

## References


Astra Zeneca (2003). Product Information Leaflet: Crestor, Rosuvastatin Calcium Tablets.

Benet, L. Z., Broccatelli, F. and Oprea, T. I. (2011). BDDCS applied to over 900 drugs. *AAPS J 13*, 519-547. doi:10.1208/s12248-011-9290-9

Bi, Y., Qiu, X., Rotter, C. J. et al. (2013). Quantitative assessment of the contribution of sodium-dependent taurocholate co-transporting polypeptide (NTCP) to the hepatic uptake of rosuvastatin, pitavastatin and fluvastatin. *Biopharm Drug Dispos 34*, 452-461. doi:10.1002/bdd.1861

Billington, S., Shoner, S., Lee, S. et al. (2019). Positron emission tomography imaging of [$^{11}$C]rosuvastatin hepatic concentrations and hepatobiliary transport in humans in the absence and presence of cyclosporin A. *Clin Pharmacol Ther 106*, 1056-1066. doi:10.1002/cpt.1506

Bosgra, S., Van De Steeg, E., Vlaming, M. L. et al. (2014). Predicting carrier-mediated hepatic disposition of rosuvastatin in man by scaling from individual transfected cell-lines in vitro using absolute transporter protein quantification and PBPK modeling. *Eur J Pharm Sci 65*, 156-166. doi:10.1016/j.ejps.2014.09.007

Boyer, J. L. (2013). Bile Formation and Secretion. In *Comprehensive Physiology* (1035-1078). Hoboken, NJ, USA: John Wiley & Sons, Inc. doi:10.1002/cphy.c120027

Chan, J. C. Y., Tan, S. P. F., Upton, Z. et al. (2019). Bottom-up physiologically-based biokinetic modelling as an alternative to animal testing. *ALTEX 36*, 597-612. doi:10.14573/altex.1812051

Chu, X., Korzekwa, K., Elsby, R. et al. (2013). Intracellular drug concentrations and transporters: Measurement, modeling, and implications for the liver. *Clin Pharmacol Ther 94*, 126-141. doi:10.1038/clpt.2013.78

Fujino, H., Saito, T., Tsunenari, Y. et al. (2004). Metabolic properties of the acid and lactone forms of HMG-CoA reductase inhibitors. *Xenobiotica 34*, 961-971. doi:10.1080/00498250400015319

Guo, Y., Chu, X., Parrott, N. J. et al. (2018). Advancing predictions of tissue and intracellular drug concentrations using in vitro, imaging and physiologically based pharmacokinetic modeling approaches. *Clin Pharmacol Ther 104*, 865-889. doi:10.1002/cpt.1183

Huang, W. and Isoherranen, N. (2018). Development of a dynamic physiologically based mechanistic kidney model to predict renal clearance. *CPT Pharmacometrics Syst Pharmacol 7*, 593-602. doi:10.1002/psp4.12321

Izumi, S., Nozaki, Y., Kusuhara, H. et al. (2018). Relative activity factor (RAF)-based scaling of uptake clearance mediated by organic anion transporting polypeptide (OATP) 1B1 and OATP1B3 in human hepatocytes. *Mol Pharm 15*, 2277-2288. doi:10.1021/acs.molpharmaceut.8b00138

Jamei, M., Bajot, F., Neuhoff, S. et al. (2014). A mechanistic framework for in vitro-in vivo extrapolation of liver membrane transporters: Prediction of drug-drug interaction between rosuvastatin and cyclosporine. *Clin Pharmacokinet 53*, 73-87. doi:10.1007/s40262-013-0097-y

Jones, H. M., Barton, H. A., Lai, Y. et al. (2012). Mechanistic pharmacokinetic modelling for the prediction of transporter-mediated disposition in human from sandwich culture human hepatocyte data. *Drug Metab Dispos 40*, 1007-1017. doi:10.1124/dmd.111.042994

Kaneko, K.-I., Tanaka, M., Ishii, A. et al. (2018). A clinical quantitative evaluation of hepatobiliary transport of [$^{11}$C] dehydropravastatin in humans using positron emission tomography. *Drug Metab Dispos 46*, 719-728. doi:10.1124/dmd.118.080408

Li, J., Volpe, D. A., Wang, Y. et al. (2011). Use of transporter knockdown Caco-2 cells to investigate the in vitro efflux of statin drugs. *Drug Metab Dispos 39*, 1196-1202. doi:10.1124/dmd.111.038075

Loreno, M., Travali, S., Bucceri, A. M. et al. (2009). Ultrasonographic study of gallbladder wall thickness and emptying in cirrhotic patients without gallstones. *Gastroenterol Res Pract 2009*, 683040. doi:10.1155/2009/683040

Martin, P. D., Mitchell, P. D. and Schneck, D. W. (2002). Pharmacodynamic effects and pharmacokinetics of a new HMG-CoA reductase inhibitor, rosuvastatin, after morning or evening administration in healthy volunteers. *Br J Clin Pharmacol 54*, 472-477. doi:10.1046/j.1365-2125.2002.01688.x

Martin, P. D., Warwick, M. J., Dane, A. L. et al. (2003). Absolute oral bioavailability of rosuvastatin in healthy white adult male volunteers. *Clin Ther 25*, 2553-2563. doi:10.1016/S0149-2918(03)80316-8

McTaggart, F., Buckett, L., Davidson, R. et al. (2001). Preclinical and clinical pharmacology of rosuvastatin, a new 3-hydroxy-3-methylglutaryl coenzyme A reductase inhibitor. *Am J Cardiol 87*, 28-32. doi:10.1016/S0002-9149(01)01454-0

Paini, A., Leonard, J. A., Joossens, E. et al. (2019). Next generation physiologically based kinetic (NG-PBK) models in support of regulatory decision making. *Comput Toxicol 9*, 61-72. doi:10.1016/j.comtox.2018.11.002

Pfeifer, N. D., Yang, K. and Brouwer, K. L. R. (2013). Hepatic basolateral efflux contributes significantly to rosuvastatin disposition I: Characterization of basolateral versus biliary clearance using a novel protocol in sandwich-cultured hepatocytes. *J Pharmacol Exp Ther 347*, 727-736. doi:10.1124/jpet.113.207472

Punt, A., Peijnenburg, A. A. C. M., Hoogenboom, R. L. A. P. et al. (2017). Non-animal approaches for toxicokinetics in risk evaluations of food chemicals. *ALTEX 34*, 501-514. doi:10.14573/altex.1702211

Riccardi, K., Lin, J., Li, Z. et al. (2017). Novel method to predict in vivo liver-to-plasma $K_{puu}$ for OATP substrates using suspension hepatocytes. *Drug Metab Dispos 45*, 576-580. doi:10.1124/dmd.116.074575

Rodgers, T., Leahy, D. and Rowland, M. (2005). Physiologically based pharmacokinetic modeling 1: Predicting the tissue distribution of moderate-to-strong bases. *J Pharm Sci 94*, 1259-1276. doi:10.1002/jps.20322

Rodgers, T. and Rowland, M. (2006). Physiologically based pharmacokinetic modelling 2: Predicting the tissue distribution of acids, very weak bases, neutrals and zwitterions. *J Pharm Sci 95*, 1238-1257. doi:10.1002/jps.20502

Rodgers, T. and Rowland, M. (2007). Mechanistic approaches to volume of distribution predictions: Understanding the processes. *Pharm Res 24*, 918-933. doi:10.1007/s11095-006-9210-3

Ryu, S., Tess, D., Chang, G. et al. (2020). Evaluation of fraction unbound across 7 tissues of 5 species. *J Pharm Sci 109*, 1178-1190. doi:10.1016/j.xphs.2019.10.060

Schirris, T. J. J., Ritschel, T., Bilos, A. et al. (2015). Statin lactonization by uridine 5′-diphospho-glucuronosyltransferases (UGTs). *Mol Pharm 12*, 4048-4055. doi:10.1021/acs.molpharmaceut.5b00474

Simonson, S. G., Raza, A., Martin, P. D. et al. (2004). Rosuvastatin pharmacokinetics in heart transplant recipients administered an antirejection regimen including cyclosporine. *Clin Pharmacol Ther 76*, 167-177. doi:10.1016/j.clpt.2004.03.010

Steffansen, B., Nielsen, C. U. and Brodin, B. (2015). Membrane Transporters in ADME. In Y. Sugiyama and B. Steffansen (eds.), *Transporters in Drug Development: Discovery, Optimization, Clinical Study and Regulation* (1-22). AAPS Advances in the Pharmaceutical Sciences Series, Volume 7. New York, NY, USA: Springer. doi:10.1007/978-1-4614-8229-1

Sun, D., Lennernas, H., Welage, L. S. et al. (2002). Comparison of human duodenum and Caco-2 gene expression profiles for 12,000 gene sequences tags and correlation with permeability of 26 drugs. *Pharm Res 19*, 1400-1416. doi:10.1023/A:1020483911355

US Food and Drug Adminstration (2020). Drug Development and Drug Interactions: Table of Substrates, Inhibitors and Inducers. https://www.fda.gov/drugs/drug-interactions-labeling/drug-development-and-drug-interactions-table-substrates-inhibitors-and-inducers#table5-1 (accessed 17.03.2020)

Verhulst, A., Sayer, R., De Broe, M. E. et al. (2008). Human proximal tubular epithelium actively secretes but does not retain rosuvastatin. *Mol Pharmacol 74*, 1084-1091. doi:10.1124/mol.108.047647

Vildhede, A., Karlgren, M., Svedberg, E. K. et al. (2014). Hepatic uptake of atorvastatin: Influence of variability in transporter expression on uptake clearance and drug-drug interactions. *Drug Metab Dispos 4*2, 1210-1218. doi:10.1124/dmd.113.056309

Wang, Q., Zheng, M. and Leil, T. (2017). Investigating transporter-mediated drug-drug interactions using a physiologically based pharmacokinetic model of rosuvastatin. *CPT Pharmacometrics Syst Pharmacol 6,* 228-238. doi:10.1002/psp4.12168

Yoshikado, T., Toshimoto, K., Nakada, T. et al. (2017). Comparison of methods for estimating unbound intracellular-to-medium concentration ratios in rat and human hepatocytes using statins. *Drug Metab Dispos 45*, 779-789. doi:10.1124/dmd.116.074823

Zhang, D., Donohue, A. F., Dragovich, P. S. et al. (2019a). Special section on pharmacokinetic and drug metabolism properties of novel therapeutic modalities catalytic cleavage of disulfide bonds in small molecules and linkers of antibody – Drug conjugates. *Drug Metab Dispos 47*, 1156-1163. doi:10.1124/dmd.118.086132

Zhang, D., Hop, C. E. C. A., Patilea-Vrana, G. et al. (2019b). Drug concentration asymmetry in tissues and plasma for small molecule-related therapeutic modalities. *Drug Metab Dispos 47*, 1122-1135. doi:10.1124/dmd.119.086744

## Conflict of interest

The authors declare that there are no conflicts of interest.

## Acknowledgement

This work was supported by SURPASS [Grant number H18/01/a0/C14] and NUS Department of Pharmacy [Grant number C-148-000-003-001]. S.P.F.T is supported by the A*STAR Graduate Academy. J.C.Y.C. and E.C.Y.C. conceived and directed the study. S.P.F.T and J.C.Y.C built the models and conducted the simulations. J.C.Y.C, S.P.F.T and E.C.Y.C wrote the manuscript.